



 Cite this: *RSC Adv.*, 2025, 15, 38562

# First-principles investigation of LiSnAl and LiSiIn half-Heusler compounds for optoelectronic applications

 Mohshina Binte Mansur,<sup>a</sup> Tasmi Akter,<sup>a</sup> Istiak Ahmed Ovi,<sup>a</sup> Jahirul Islam <sup>\*,a</sup> and Wahidur Rahman Sajal<sup>\*,ab</sup>

This study presents a comprehensive first-principles investigation into the structural, electrical, magnetic, mechanical, optical, and thermodynamic properties of two lithium-based half-Heusler semiconductors, LiSiIn and LiSnAl. Our findings confirm that both LiSiIn and LiSnAl possess a cubic C1b crystal structure ( $F\bar{4}3m$  space group) and satisfy Born's stability criteria, confirming their mechanical stability. They exhibit indirect and narrow band gaps of 0.095 eV (LiSnAl) and 0.228 eV (LiSiIn) with GGA-PBE, and 0.517 eV (LiSnAl) and 0.591 eV (LiSiIn) with HSE06, indicating semiconducting behavior. Charge density and Mulliken population analyses reveal a mixed ionic-covalent bonding, while negative Cauchy pressure indicates brittleness. LiSiIn demonstrates superior stiffness, deformation resistance, and fracture strength compared to LiSnAl. Optically, both compounds exhibit high dielectric constants, UV reflectivity (56–60%), and strong low-energy absorption, suggesting potential applications in capacitors, photovoltaics, and thermophotovoltaics. Phonon dispersion confirms dynamic stability, and thermodynamic results show low minimum thermal conductivities ( $\sim 0.006$ – $0.007$  W m<sup>-1</sup> K<sup>-1</sup>) and high melting points (1003.46 K for LiSnAl, 1100.02 K for LiSiIn). The higher melting point of LiSiIn reflects stronger bonding, while LiSnAl's lower thermal conductivity favors thermal energy storage. Overall, both materials demonstrate multifunctional potential for next-generation energy and optoelectronic devices.

 Received 4th July 2025  
 Accepted 4th October 2025

DOI: 10.1039/d5ra04779j

[rsc.li/rsc-advances](http://rsc.li/rsc-advances)

## 1 Introduction

In the pursuit of sustainable development and environmental protection, the transition towards clean and renewable energy sources has become imperative. The increasing reliance on fossil fuels has led to critical issues such as fuel scarcity and environmental degradation, further worsened by the widespread use of electronic appliances like refrigerators and air conditioners, which contribute significantly to greenhouse gas emissions.<sup>1</sup> To address these challenges, researchers are exploring green and eco-friendly energy conversion technologies. Among them, thermoelectric materials have attracted considerable attention due to their ability to convert waste heat—generated from sources such as automobiles, industrial processes, and power plants—into electrical energy, thereby offering a viable solution to the global energy crisis.<sup>2–4</sup>

Half-Heusler compounds have emerged as promising candidates for thermoelectric and other energy-efficient

applications due to their excellent electrical conductivity, moderate thermal conductivity, and mechanical robustness. These ternary intermetallic compounds, typically with the general formula XYZ, have shown great potential in various advanced technologies including spintronics, superconductivity, photovoltaics, topological insulators, capacitors, and high-temperature semiconductors.<sup>5</sup> The flexibility in band structure engineering further enhances their appeal across a wide spectrum of electronic and optoelectronic applications. Various thermoelectric materials such as GeTe,<sup>6</sup> Bi<sub>2</sub>Te<sub>3</sub>,<sup>7</sup> PbTe,<sup>8,9</sup> and half-Heusler<sup>10</sup> alloys are actively being investigated for their potential in power generation and cooling technologies.

Half-Heusler compounds typically crystallize in the cubic C1b structure or its hexagonal variant, with specific atomic arrangements at Wyckoff positions (*e.g.*, 4a, 4b, 4c) that significantly influence their stability and electronic properties.<sup>11–13</sup> Understanding these atomic configurations is crucial for tuning the physical properties and optimizing performance for targeted applications.<sup>14,15</sup> Of particular interest are eight-electron Li-based half-Heusler compounds, where the high electronegativity of elements Y and Z facilitates electron transfer from the electropositive element X (*e.g.*, Li), resulting in semiconducting behavior with tunable direct or indirect band gaps. These

<sup>a</sup>Department of Materials Science and Engineering, Khulna University of Engineering & Technology, Khulna-9203, Bangladesh. E-mail: jahirul@mse.kuet.ac.bd; wrsajal@nce.buet.ac.bd

<sup>b</sup>Department of Nanomaterials and Ceramic Engineering, Bangladesh University of Engineering and Technology, Dhaka-1000, Bangladesh



materials are known for their favorable optical, mechanical, and electronic properties, making them suitable for a wide range of technologies including photovoltaics, sensors, and thermoelectric devices.<sup>16–18</sup>

Lithium-based half-Heusler compounds, in particular, offer several advantages: they are lightweight, abundant, non-toxic, and cost-effective, making them attractive for large-scale energy applications. Their optical properties, especially high absorption coefficients and interband transition capabilities, make them excellent candidates for optoelectronic and photonic devices.<sup>4,19</sup> Vikram *et al.*<sup>11</sup> demonstrated that LiSnAl and LiSiIn compounds exhibit high thermoelectric performance, with a figure of merit (ZT) exceeding 0.8 for n-type and above 0.5 for p-type doping, indicating strong potential for efficient thermoelectric energy conversion. These compounds also showed high power factors, underscoring their suitability for thermoelectric generator (TEG) applications.

The adjustable band gap of lithium-based half-Heusler alloys makes them highly intriguing for photonic and optical purposes. These alloys exhibit a notable capacity for photon absorption *via* interband transitions, and their substantial absorption coefficient positions them as promising candidates for energy-efficient semiconductor materials in power device applications. Given their excellent optical response, half-Heusler alloys are the top choice for optical and thermoelectric applications.<sup>4,19</sup>

Existing studies further suggest that larger atomic sizes can lead to reduced band gaps, as seen in LiSnAl compared to its counterparts, such as LiAlGe and LiAlSi.<sup>20</sup> Mechanical assessments of similar compounds reveal a brittle nature, which aligns with the characteristics observed in LiSiIn and LiSnAl. The calculated Debye temperature of LiSiIn is consistent with previously studied half-Heusler compounds like AlNiP,<sup>21</sup> while trends in lattice constants and bulk moduli in analogous systems (*e.g.*, LiSrN, LiSrP, LiSrAs) confirm size-related effects on mechanical stability.<sup>14</sup> Minhajul Islam *et al.*<sup>22</sup> investigated XCrAl (X = Fe, Co, Ni, Cu) half-Heusler alloys for optoelectronic and high-temperature applications, reinforcing the suitability of such systems for advanced functional devices. Furthermore, lithium-based compounds such as LiBeAs, LiScSb, and LiGeBi have demonstrated excellent optical responses, strengthening the case for their use in optoelectronics.<sup>23</sup>

Despite their potential, the properties of LiSnAl and LiSiIn remain underexplored. This study aims to fill that gap by conducting a comprehensive first-principles investigation into their structural, optical, electronic, mechanical, and bonding characteristics. These materials, due to their low atomic mass and high carrier mobility, offer promising avenues for controlling thermal conductivity and enhancing light absorption key traits for thermoelectric, IR detectors and thermophotovoltaics devices. Our findings provide fundamental insights into their multifunctional behavior and assess their viability for next-generation energy applications such as photovoltaics, capacitors, topological insulators, and field-effect transistors. Through this work, we aim to elucidate whether these materials merit further experimental validation and technological development.

## 2 Computational methods

First-principles calculations based on density functional theory (DFT) were performed using the Cambridge Serial Total Energy Package (CASTEP) module. All computations were carried out within the framework of the Generalized Gradient Approximation (GGA), employing the Perdew–Burke–Ernzerhof (PBE) exchange–correlation functional. CASTEP facilitates quantum mechanical simulations to investigate the structural, electronic, optical, mechanical, and thermal properties of a wide range of materials, including semiconductors, ceramics, metals, minerals, and zeolites.<sup>24</sup> Before the property analysis, geometry optimization was conducted to refine the atomic configuration of the three-dimensional periodic system and achieve a stable structure. The CASTEP module enables the examination of material properties under hydrostatic pressure and supports various constraint options, with atomic position fixation being the most fundamental.<sup>25</sup> Among the available minimization algorithms, the Broyden–Fletcher–Goldfarb–Shanno (BFGS) method<sup>26</sup> generally provides a faster convergence rate, whereas the LBFGS (limited-memory BFGS) algorithm is better suited for large systems due to its improved computational efficiency. Following the structure optimization, the material's structural, mechanical, electronic, optical, and thermal properties were systematically evaluated. To describe the interaction between electrons and atomic nuclei, ultrasoft pseudopotentials were employed. A plane-wave cutoff energy of 450 eV was selected for the basis set expansion. Brillouin zone sampling was carried out using a  $15 \times 15 \times 15$  Monkhorst–Pack *k*-point mesh,<sup>27</sup> which is critical for accurate ground-state calculations, including self-consistent field (SCF) convergence.<sup>28</sup> Convergence thresholds were rigorously maintained, with total energy differences constrained to within  $1 \times 10^{-5}$  eV per atom, maximum Hellmann–Feynman forces limited to  $0.03 \text{ eV } \text{Å}^{-1}$ , maximum atomic displacements restricted to  $0.01 \text{ Å}$ , and maximum stress capped at 0.05 GPa. Spin polarization was incorporated using the collinear approximation during geometry optimization to evaluate the magnetic behavior of the studied compounds. For optical property calculations, a denser *k*-point mesh of  $14 \times 14 \times 14$  was adopted to ensure greater accuracy. The electronic properties were determined using the same computational parameters as those used in geometry optimization. The elastic stiffness constants ( $C_{ij}$ ) were calculated using the stress–strain method, from which the Debye temperature and sound velocities were subsequently derived.<sup>29</sup> Furthermore, phonon calculations enabled the evaluation of thermodynamic quantities, including specific heat capacity ( $C_v$ ), entropy as a function of temperature, and the variation of Debye temperature, over a temperature range of 10 K to 800 K.

## 3 Results and discussion

### 3.1 Structural properties

In this study, the structural characteristics of the half-Heusler alloys LiSiIn and LiSnAl were systematically investigated. Both compounds crystallize in the cubic C1b-type structure, which belongs to the  $F\bar{4}3m$  space group (space group no. 216). Among



the various configurations of Heusler compounds, the C1b-type cubic structure is the most prevalent, typically characterized by a 1 : 1 : 1 stoichiometric atomic ratio. The electronic configurations of the valence shells for the constituent elements are as follows: Li ( $2s^1$ ), Si ( $3s^2 3p^2$ ), Al ( $3s^2 3p^1$ ), In ( $5s^2 5p^1$ ), and Sn ( $5s^2 5p^2$ ). Within the unit cell, the atomic positions are assigned such that the X, Y, and Z elements occupy the fractional coordinates (0.0, 0.0, 0.0), (0.25, 0.25, 0.25), and (0.50, 0.50, 0.50), respectively. The lattice parameters for LiSiIn and LiSnAl were initially reported as 6.31 Å and 6.47 Å, respectively, in previous literature. In the present work, geometry optimization was carried out using the GGA-PBE functional. The optimized lattice parameters were found to be 6.284 Å for LiSiIn and 6.473 Å for LiSnAl. These values show excellent agreement with earlier results, with deviations of approximately 0.41% for LiSiIn and a negligible 0.0003% for LiSnAl. Table 1 presents the calculated lattice constants and unit cell volumes for both compounds. As observed, LiSnAl exhibits a comparatively larger lattice constant and unit cell volume than LiSiIn, which is consistent with the atomic radii of the constituent elements. The optimized structures and corresponding lattice constants are illustrated in

**Table 1** The calculated lattice constant and unit cell volume of Li-based half-Heusler

| Compound | Lattice parameter, $a$ (Å) |                             | Cell volume (Å <sup>3</sup> ) |
|----------|----------------------------|-----------------------------|-------------------------------|
|          | This work                  | Previous work <sup>11</sup> |                               |
| LiSnAl   | 6.473                      | 6.47                        | 271.17                        |
| LiSiIn   | 6.284                      | 6.31                        | 248.19                        |

Fig. 1, confirming the structural stability and convergence of geometry optimization. The identification of the most energetically favorable structure is consistent with previous theoretical predictions.

### 3.2 Electronic properties

The electronic characteristics of LiSnAl and LiSiIn half-Heusler compounds were thoroughly investigated through the analysis of their electronic band structures (EBS) and density of states (DOS). These tools offer crucial insights into the electronic behavior of materials, particularly with respect to their semi-conducting nature and potential for energy applications. The electronic band structures of LiSnAl and LiSiIn *via* GGA-PBE functional were computed along high-symmetry directions in the Brillouin zone, as illustrated in Fig. 2(a) and (b). As the GGA-PBE functional underestimates the bandgap values, the band structure was also calculated with Hybrid-HSE06 functional for more accuracy, illustrated in Fig. 3(a) and (b). The energy dispersion is plotted with respect to the Fermi energy,  $E_F$ , spanning a range from  $-6$  eV to  $+6$  eV. The Fermi level is denoted by a horizontal red dashed line positioned at 0 eV. Our calculations reveal that both the valence band maximum (VBM) and the conduction band minimum (CBM) are located at the  $\Gamma$ -point, indicating that LiSnAl and LiSiIn are direct band gap semiconductors. The calculated band gap values are 0.228 eV for LiSnAl and 0.095 eV for LiSiIn, which are in good agreement with prior theoretical studies, where values of 0.26 eV and 0.13 eV were reported, respectively.<sup>11</sup> Using the Hybrid-HSE06 functional, the calculated bandgaps were found 0.517 eV and 0.591 eV for the LiSnAl and LiSiIn compounds, respectively. The slight

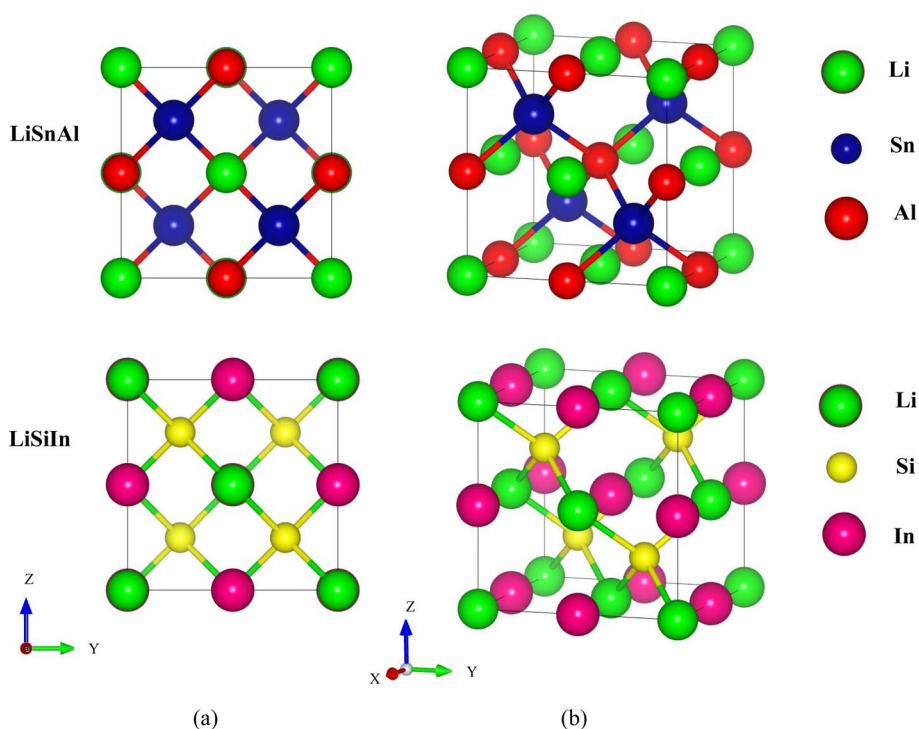


**Fig. 1** The optimized conventional (a) 2D and (b) 3D ball & stick model unit cell crystal structure for LiSnAl and LiSiIn compounds.



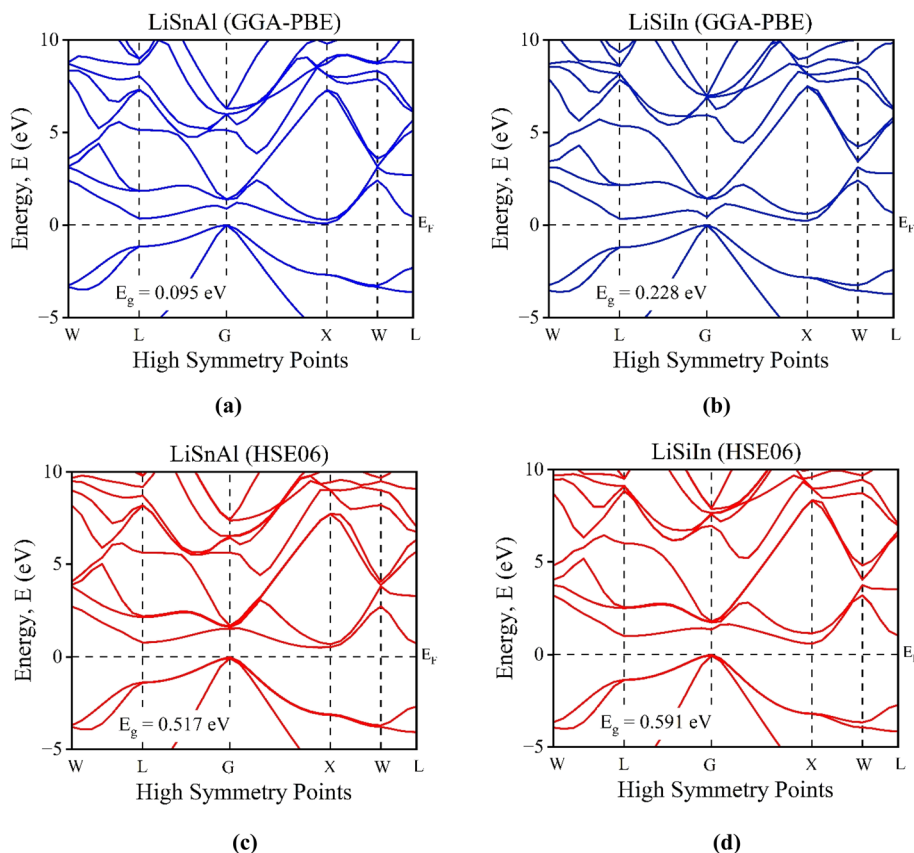


Fig. 2 The calculated electronic band structure (EBS) of the half-Heusler compounds with GGA-PBE and Hybrid-HSE06 functionals [(a) LiSnAl with GGA-PBE, (b) LiSiIn with GGA-PBE, (c) LiSnAl with Hybrid-HSE06 (d) LiSiIn with Hybrid-HSE06].

discrepancies are attributed to differences in computational methodologies was employed in the present study, whereas the reference utilized VASP. Despite this, the overall trends are consistent and reaffirm the semiconducting nature of these compounds. Moreover, the proximity of the Fermi level to the valence band edge suggests a p-type semiconducting behavior.<sup>30</sup> The spin-polarized calculations were performed to check for possible magnetic behavior. Our results show that the up- and down-spin channels are fully degenerate in the electronic ground state, indicating that the compounds studied are non-magnetic. Consequently, only the spin-up band structures and density of states (DOS) are presented, as the spin-down channels are identical.

The corresponding total and partial density of states (TDOS and PDOS) are depicted in Fig. 3 using GGA-PBE and Hybrid-HSE06 functional, respectively, with the Fermi level again marked at 0 eV. The TDOS clearly distinguishes the valence and conduction bands, situated to the left and right of the Fermi level, respectively. The PDOS analysis reveals that the p-orbitals of Al, Si, In, and Sn contribute significantly near the Fermi level, particularly in both the valence and conduction bands. The s-orbital of Li also contributes, albeit to a lesser extent, indicating orbital hybridization. In the case of LiSiIn, a broad peak within the energy window from approximately  $-1.4$  eV to  $3.3$  eV can be attributed predominantly to the Li-p, Si-p, and In-p states, while

minor contributions arise from Li-s, Si-s, and In-s orbitals. Similarly, in LiSnAl, the Sn-p and Al-p states dominate near the band edges. Notably, strong p-d orbital hybridization involving In and Sn occurs in the energy range of 0.5 to 1.8 eV, playing a crucial role in shaping the electronic structure. The observed hybridization effects arise from the interaction of atoms within the crystal lattice, which results in mixed orbital character and delocalization of electronic states, a key feature in solid-state physics that enhances the material's transport and thermoelectric properties. These electronic features underline the potential of LiSiIn and LiSnAl as semiconducting materials suitable for thermoelectric applications. Their direct band gap, tunable electronic structure, and hybridized states are especially promising for enhancing charge carrier transport and optimizing thermoelectric performance.<sup>31</sup>

### 3.3 Charge density and Mulliken population analysis

To gain insights into the nature of chemical bonding in the LiSiIn and LiSnAl half-Heusler compounds, charge density distribution (CDD) analyses were performed. The charge density maps were generated along the (111) crystallographic plane for LiSiIn and the (101) plane for LiSnAl, as illustrated in Fig. 4. These plots provide valuable visual evidence for distinguishing between ionic, covalent, or mixed bonding characteristics. In the visualizations, the electron density is



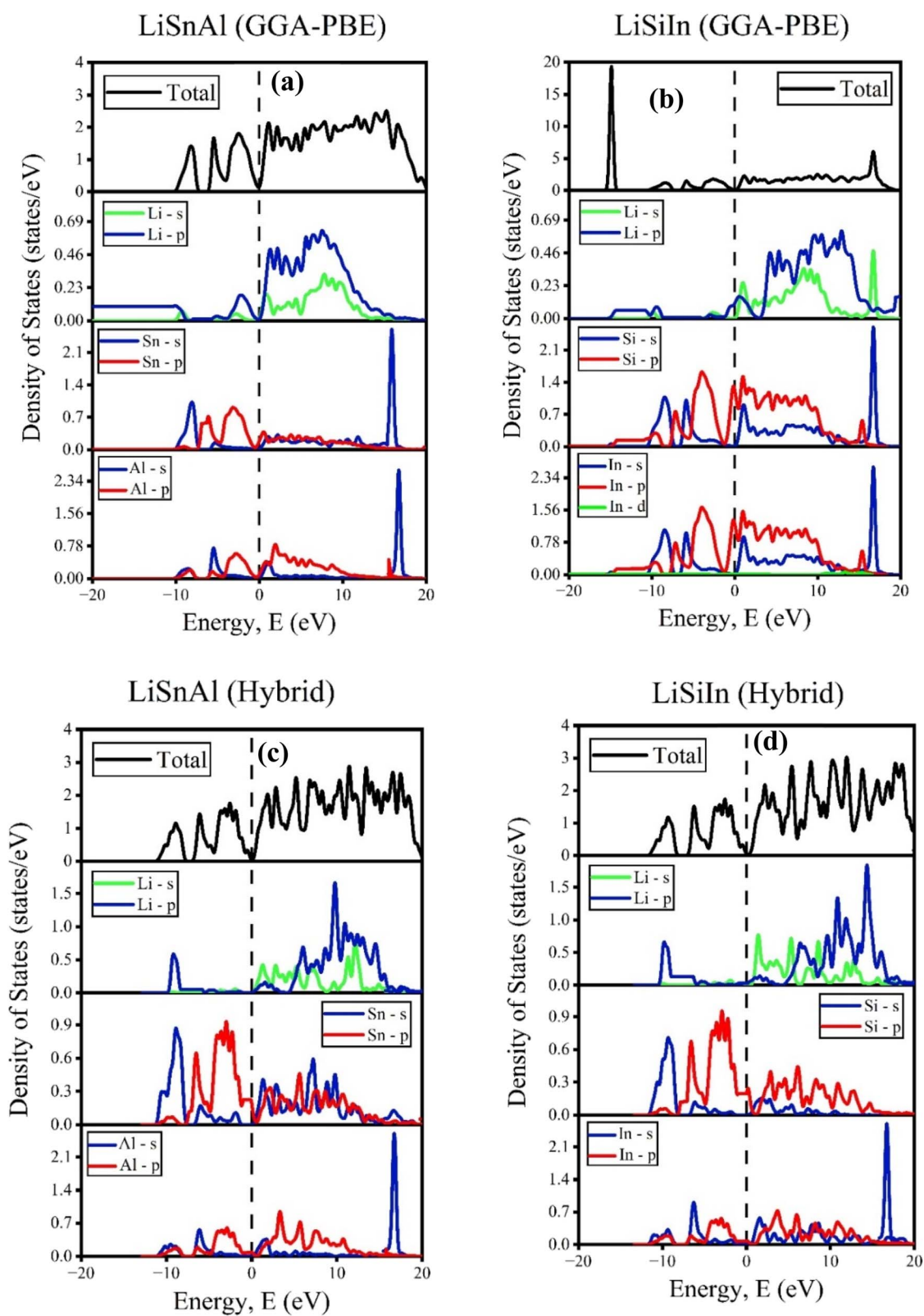


Fig. 3 The Total Density of States (TDOS) and partial density of states (PDOS) of LiSnAl and LiSiIn compounds via GGA-PBE and Hybrid-HSE06 functionals [(a) LiSnAl with GGA-PBE, (b) LiSiIn with GGA-PBE, (c) LiSnAl with Hybrid-HSE06 (d) LiSiIn with Hybrid-HSE06].



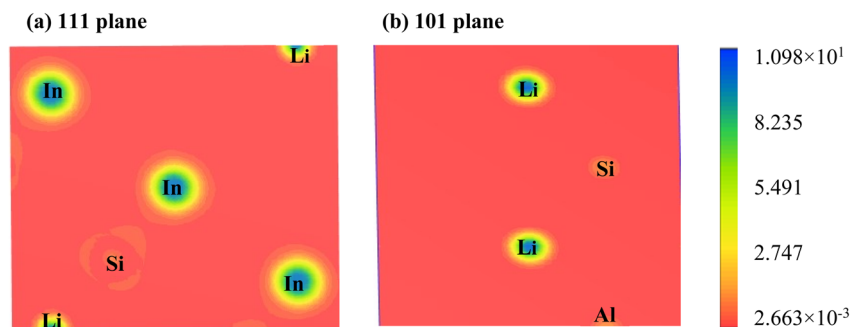


Fig. 4 The electronic charge density distribution mapping for LiSiIn and LiSnAl in individual planes (a) (111) and (b) (101).

Table 2 The calculated atomic population and charge distribution (Mulliken) of LiSnAl and LiSiIn

| Compound | Atom | Mulliken atomic population |      |      |      | Total | Formal charge | Charge ( <i>e</i> ) | Effective valence (EV) |
|----------|------|----------------------------|------|------|------|-------|---------------|---------------------|------------------------|
|          |      | s                          | p    | d    | f    |       |               |                     |                        |
| LiSnAl   | Li   | 2.06                       | 0.54 | 0.00 | 0.00 | 2.59  | +1            | 0.41                | 0.59                   |
|          | Sn   | 1.30                       | 3.10 | 0.00 | 0.00 | 4.40  | +4            | −0.40               | 4.4                    |
|          | Al   | 1.19                       | 1.82 | 0.00 | 0.00 | 3.00  | +3            | −0.00               | 3.0                    |
| LiSiIn   | Li   | 1.95                       | 0.49 | 0.00 | 0.00 | 2.43  | +1            | 0.57                | 0.43                   |
|          | Si   | 1.53                       | 3.15 | 0.00 | 0.00 | 4.67  | −4            | −0.67               | −3.36                  |
|          | In   | 1.14                       | 1.77 | 9.98 | 0.00 | 12.89 | +3            | 0.11                | 2.89                   |

represented using a color gradient scale—blue regions indicate high electron density, while red regions denote areas of low electron concentration. The CDD of both compounds reveals spherical charge contours around the Li and In (or Sn) atoms, with a clear lack of orbital overlap between these atomic centers. This observation is indicative of a predominantly ionic character in the bonding between these atoms.<sup>4,32</sup> In particular, Fig. 4(b) shows that Al exhibits minimal electron density (represented in red), while Li contributes significantly (blue), and Sn has a relatively small influence (light orange), reinforcing the ionic interpretation.

Mulliken population<sup>33</sup> analysis further supports these findings, with calculated atomic charges of +0.57 (Li), −0.67 (Si), and +0.11 (In) for LiSiIn, and +0.41 (Li), −0.40 (Sn), and ~0.00 (Al) for LiSnAl, as listed in Table 2, suggesting that Li atoms lose electrons (ionic behavior). At the same time, Si and Sn gain partial negative charges (partial covalent contributions). These values suggest that Li atoms lose electrons (ionic behavior), while Si and Sn gain partial negative charges (partial covalent contributions). In particular, the small positive charge on In arises from its 5p states, indicating d-orbital involvement and a slight metallic character.

The Mulliken population analysis highlights that the bonding in these half-Heusler compounds cannot be classified as purely ionic or covalent, but instead exhibits a mixed ionic-covalent character. The presence of d-orbital participation in In further suggests a degree of metallic character in the bonding, especially in LiSiIn. The slight distortion of spherical contours between Si and In in Fig. 4 supports this hybrid nature, indicating a localized orbital overlap and suggesting partial

covalency. However, no significant overlap is observed between Li and In/Sn, reinforcing their ionic interaction. Furthermore, the effective valence charge—calculated by subtracting the formal ionic charge from the Mulliken charge—provides quantitative insight into the bond character. An effective valence of zero corresponds to a purely ionic bond, while positive values imply increasing covalency.<sup>34</sup> In both compounds, deviations from formal ionic charges reflect charge delocalization and orbital hybridization, which are essential for understanding the electronic structure, bonding stability, and transport properties of these materials. Overall, the combination of charge density mapping and Mulliken population analysis affirms that LiSiIn and LiSnAl exhibit predominantly ionic bonding between Li and the other elements, with moderate covalent and metallic contributions arising from the interaction of p- and d-orbitals in In, Al, and Si/Sn.

These mixed bonding characteristics are expected to significantly influence the electronic, optical, and thermoelectric behaviors of the compounds. Moreover, the outcomes of the partial density of states (PDOS) analysis align with the observation that indium and lithium exhibit the most substantial charge density contributions.

### 3.4 Mechanical properties

To evaluate the elastic properties of the investigated half-Heusler alloys, the elastic constants were calculated by determining the stress tensors for a set of systematically deformed structures. Using the elastic constants task the full second-order elastic stiffness tensor ( $6 \times 6$  matrix) for each three-dimensional periodic system was obtained. The mechanical stability



of these materials was assessed based on the Born mechanical stability criteria, which are expressed by the following conditions for cubic systems,<sup>35</sup>

$$C_{11} > 0; C_{44} > 0; C_{11} > C_{12} \quad (3.1)$$

$$C_{11} + 2C_{12} > 0; C_{12} < B < C_{11} \quad (3.2)$$

The elastic constants reveal valuable insights into the mechanical behavior of the compounds. The longitudinal stiffness is represented by  $C_{11}$ , shear resistance by  $C_{44}$ , and the off-diagonal elastic coupling by  $C_{12}$ .<sup>36</sup> The calculated elastic constants for both LiSnAl and LiSiIn satisfy the above conditions, confirming their mechanical stability.

To estimate the elastic moduli of polycrystalline materials from single-crystal data, the Voigt, Reuss, and Hill (VRH) averaging schemes were employed.<sup>37,38</sup> These schemes provide upper (Voigt) and lower (Reuss) bounds, and their arithmetic mean (Hill average) is widely accepted as a realistic estimate. The relevant elastic parameters, including bulk modulus ( $B$ ), shear modulus ( $G$ ), Young's modulus ( $E$ ), Poisson's ratio ( $\nu$ ), Pugh's ratio ( $B/G$ ), and anisotropy factor ( $A$ ), were calculated using the following equations:<sup>37</sup>

$$B_V = B_R = 1/3 (C_{11} + 2C_{12}) \quad (3.3)$$

$$G_R = \frac{5(C_{11} - C_{12})C_{44}}{3(C_{11} - C_{12}) + 4C_{44}} \quad (3.4)$$

$$G_V = 1/5 (C_{11} - C_{12} + 3C_{44}) \quad (3.5)$$

$$G = 1/2 (G_V + G_R) \quad (3.6)$$

$$A = \frac{2C_{44}}{C_{11} - C_{12}} \quad (3.7)$$

From the calculated bulk and shear moduli, other mechanical parameters, including Young's modulus  $E$  and the Poisson ratio  $\nu$ , Pugh's ratio were derived as follows,<sup>38</sup>

$$\text{Young Modulus, } E = \frac{9BG}{3B + G} \quad (3.8)$$

$$\text{Poisson ratio, } \nu = (3B - 2G)/2(3B + G) \quad (3.9)$$

$$\text{Pugh ration, } p = B/G \quad (3.10)$$

Comparison of bulk modulus ( $B$ ), shear modulus ( $G$ ), and Young modulus ( $E$ ) for LiSiIn and LiSnAl are shown in Fig. 5 and all mechanical properties are listed in Table 3. The bulk modulus ( $B$ ) serves as a measure of a material's resistance to uniform compression. Notably, LiSiIn exhibits a higher bulk modulus than LiSnAl, indicating superior resistance to volumetric deformation and enhanced overall stiffness. Young's modulus ( $E$ ), which defines the ratio of tensile stress to tensile strain, also reflects the rigidity of the material.<sup>39</sup> The  $E$  values suggest that LiSiIn is stiffer than LiSnAl.  $G_V$  indicates the top bound of shear modulus under uniform strain assumptions, while  $G_R$  represents the lower bound under uniform stress

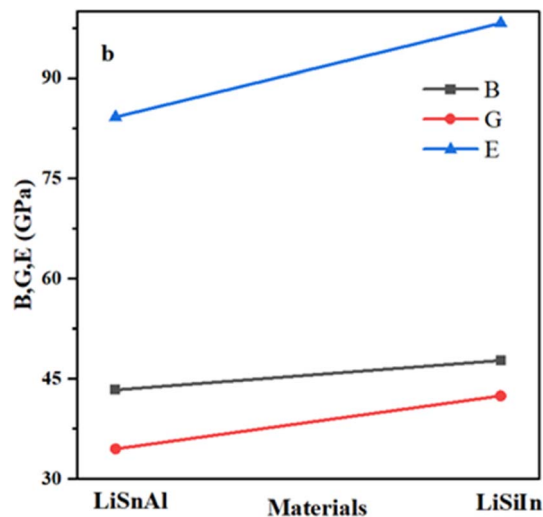


Fig. 5 The comparison of Shear modulus ( $G$ ), Bulk modulus ( $B$ ), and Young modulus ( $E$ ) for LiSiIn and LiSnAl.

Table 3 The determined elastic parameters (GPa) for cubic LiSnAl and LiSiIn half-Heusler alloys at their equilibrium volume

| Parameters                         | LiSnAl | LiSiIn |
|------------------------------------|--------|--------|
| $C_{11}$                           | 76.22  | 92.56  |
| $C_{12}$                           | 26.92  | 26.37  |
| $C_{44}$                           | 43.2   | 49.63  |
| Young's modulus, $E$               | 84.19  | 98.24  |
| Bulk modulus, $B$                  | 43.35  | 47.76  |
| Shear modulus, $G$                 | 34.49  | 42.45  |
| Poisson ratio, $\nu$               | 0.185  | 0.157  |
| Anisotropy factor, $A$             | 1.75   | 1.47   |
| Cauchy pressure, $C_{12} - C_{44}$ | -16.2  | -23.6  |
| Pugh's ratio, $B/G$                | 1.25   | 1.12   |

circumstances. The shear modulus ( $G$ ), indicative of resistance to shape deformation, further corroborates this conclusion, with LiSiIn (42.45 GPa) outperforming LiSnAl (34.49 GPa). This implies that LiSiIn is more resistant to plastic deformation and fracture.<sup>40</sup>

Pugh's ratio ( $B/G$ ) is widely used to predict ductility or brittleness. A  $B/G$  value above 1.75 suggests ductile behavior, whereas a lower value indicates brittleness.<sup>41,42</sup> The computed  $B/G$  values (1.25 for LiSnAl and 1.12 for LiSiIn) clearly classify both materials as brittle. These results are consistent with reported values for other half-Heusler alloys such as LiAlGe, LiAlSi, and YCrSb.

The Poisson's ratio ( $\nu$ ), which quantifies the transverse strain response to axial stress, typically ranges from 0.25 to 0.50 in solids. The calculated values for LiSnAl (0.185) and LiSiIn (0.157) fall below this range, indicating that non-central interatomic forces dominate. These values suggest a bonding nature that includes significant covalent character. According to ref. 45, a Poisson's ratio below 0.10 indicates pure covalent bonding, while values above 0.33 indicate metallic bonding.



Hence, these alloys exhibit a mixed ionic-covalent bonding character. This is further confirmed by the negative Cauchy pressures ( $C_{12}$ – $C_{44}$ ), which are also indicators of covalent bonding and mechanical brittleness.<sup>43</sup>

The machinability index, defined as  $\mu_m = B/C_{44}$ , provides insights into the material's plastic deformation and lubrication behavior.<sup>44</sup> LiSnAl shows a relatively higher machinability index ( $\sim 1$ ), implying its better plasticity under machining conditions. This parameter is crucial in manufacturing and tool design, affecting cutting speed, geometry, and force.

Finally, the anisotropy factor ( $A$ ) reflects the directional dependence of elastic properties. A value of  $A = 1$  indicates isotropy, while values different from 1 imply anisotropy.<sup>47,48</sup> The calculated anisotropy factors (1.75 for LiSnAl and 1.47 for LiSiIn) suggest that both compounds exhibit significant elastic anisotropy, which can influence crack propagation and fracture behavior under stress.

### 3.5 Optical properties

To obtain accurate optical properties, we employed a dense Monkhorst–Pack  $k$ -mesh of  $14 \times 14 \times 14$ . The complex dielectric function, expressed as  $\varepsilon_1(\omega) = \varepsilon_1(\omega) + i\varepsilon_2(\omega)$ , comprises a real part  $\varepsilon_1(\omega)$  and an imaginary part  $\varepsilon_2(\omega)$ , which characterize the dispersion and absorption behaviors of the material, respectively.<sup>46</sup> The real component  $\varepsilon_1(\omega)$  can be derived from  $\varepsilon_2(\omega)$  via the Kramers–Kronig transformation  $\varepsilon_2(\omega)$ , as shown in eqn (3.11):

$$\varepsilon_1(\omega) = 1 + \frac{2}{\pi} P \int_0^{\infty} \frac{\omega' \varepsilon_2(\omega')}{\omega'^2 - \omega^2} d\omega' \quad (3.11)$$

The imaginary part  $\varepsilon_2(\omega)$  is calculated based on the momentum matrix elements between occupied and unoccupied electronic states, using the following formulation:

$$\varepsilon_2(\omega) = \frac{2e^2\pi}{\Omega\varepsilon_0} \sum_{k,v,c} \left| \langle \psi_k^c | \hat{U} | \vec{r} | \psi_k^v \rangle \right|^2 \delta(E_k^c - E_k^v - E) \quad (3.12)$$

Here,  $\psi_k^c$  and  $\psi_k^v$  are the conduction and valence band wavefunctions at wavevector  $k$ ,  $e$  is the elementary charge,  $\Omega$  is the unit cell volume,  $\varepsilon_0$  is the vacuum permittivity, and  $\hat{U}$  is the polarization direction of the incident electric field. The delta function enforces energy conservation during photon-induced electronic transitions.<sup>47,48</sup>

From the calculated  $\varepsilon_1$  and  $\varepsilon_2$ , various optical constants can be derived, such as the absorption coefficient  $\alpha(\omega)$ , refractive index  $n(\omega)$ , reflectivity  $R(\omega)$ , optical conductivity, and the electron energy loss function  $L(\omega)$ . These parameters provide valuable insights into the electronic structure and light–matter interactions within the material.

Our focus is restricted to interband transitions, as intraband contributions are negligible in semiconductors. The static dielectric constant  $\varepsilon_1(0)$  is especially significant in thermophotovoltaic applications, as higher values typically enhance the material's suitability for dielectric and photovoltaic uses. The computed static dielectric constants are approximately 24 and 26 for LiSnAl and LiSiIn, respectively, as shown in Fig. 6(a).

These elevated values suggest excellent performance in applications like capacitors and IR detector devices. In the energy range of 2.8–3.15 eV, both compounds exhibit a decline in dielectric behavior, indicating a transition from energy storage to energy absorption (heat dissipation). Peaks in the imaginary part  $\varepsilon_2(\omega)$  occur at approximately 2.58 eV for LiSnAl and 2.92 eV for LiSiIn, as depicted in Fig. 6(b). These features arise from transitions involving Sn-p and Si-p valence states, respectively, and lie within the visible spectrum, suggesting suitability for photovoltaic applications.

The refractive index, illustrated in Fig. 6(c), indicates how light propagates through the materials. For both compounds,  $n(0)$  is found to be  $\sim 4.9$  for LiSnAl and  $\sim 5.0$  for LiSiIn, peaking in the infrared region and decreasing monotonically through the visible spectrum. This optical behavior is advantageous for devices like antireflective coatings, optical filters, and photodetectors.

Reflectivity spectra, shown in Fig. 6(d), reveal reflectance values between 56–60% in the visible range, indicating potential for solar radiation mitigation. In the UV region, both materials exhibit high reflectance—71% for LiSiIn at  $\sim 7.8$  eV and 73% for LiSnAl at  $\sim 8.0$  eV—coinciding with a drop in absorption and highlighting their reflective nature in this range.

The absorption spectra in Fig. 7(a) starts from zero, confirming their semiconducting nature. LiSiIn demonstrates a significant absorption peak in the UV range (4–5 eV), indicating strong ultraviolet absorption. The corresponding wavelength curves in Fig. 7(b) show active absorption between 280–330 nm for both materials, confirming their capability to absorb UV radiation. Refractive index values between 2–3 and reflectivity below 40% further suggest their suitability for high-transparency applications with minimal energy loss.

Fig. 8(a), (b), and (c) display the optical conductivity and electron energy loss spectra. The optical conductivity closely follows the absorption profile, with photoconductivity onset observed at photon energies as low as  $\sim 0.1$ – $0.2$  eV for both compounds, implying a narrow band gap. In particular, LiSnAl shows a pronounced conductivity rise within the visible spectrum (up to  $\sim 2.86$  eV), aligning with efficient light absorption in the 300–450 nm range.<sup>49</sup>

Fig. 8(c) presents the frequency-dependent energy loss function  $L(\omega)$ , a critical parameter describing the energy loss experienced by fast electrons traversing the material. The most prominent peak corresponds to plasma resonance, representing collective oscillations of electrons. For both compounds, significant peaks appear in the UV range (10.5–13.5 eV), denoting the plasma frequency. These peaks coincide with sharp declines in reflectivity (Fig. 8(d)) and absorption (Fig. 9(a)), confirming the interrelated nature of these optical properties.<sup>55–57</sup>

In summary, the optical analyses indicate that LiSnAl and LiSiIn half-Heusler compounds possess promising characteristics for use in UV photodetectors, optical filters, and other thermophotovoltaics applications due to their high refractive index, strong UV absorption, low reflectivity, and favorable dielectric response.





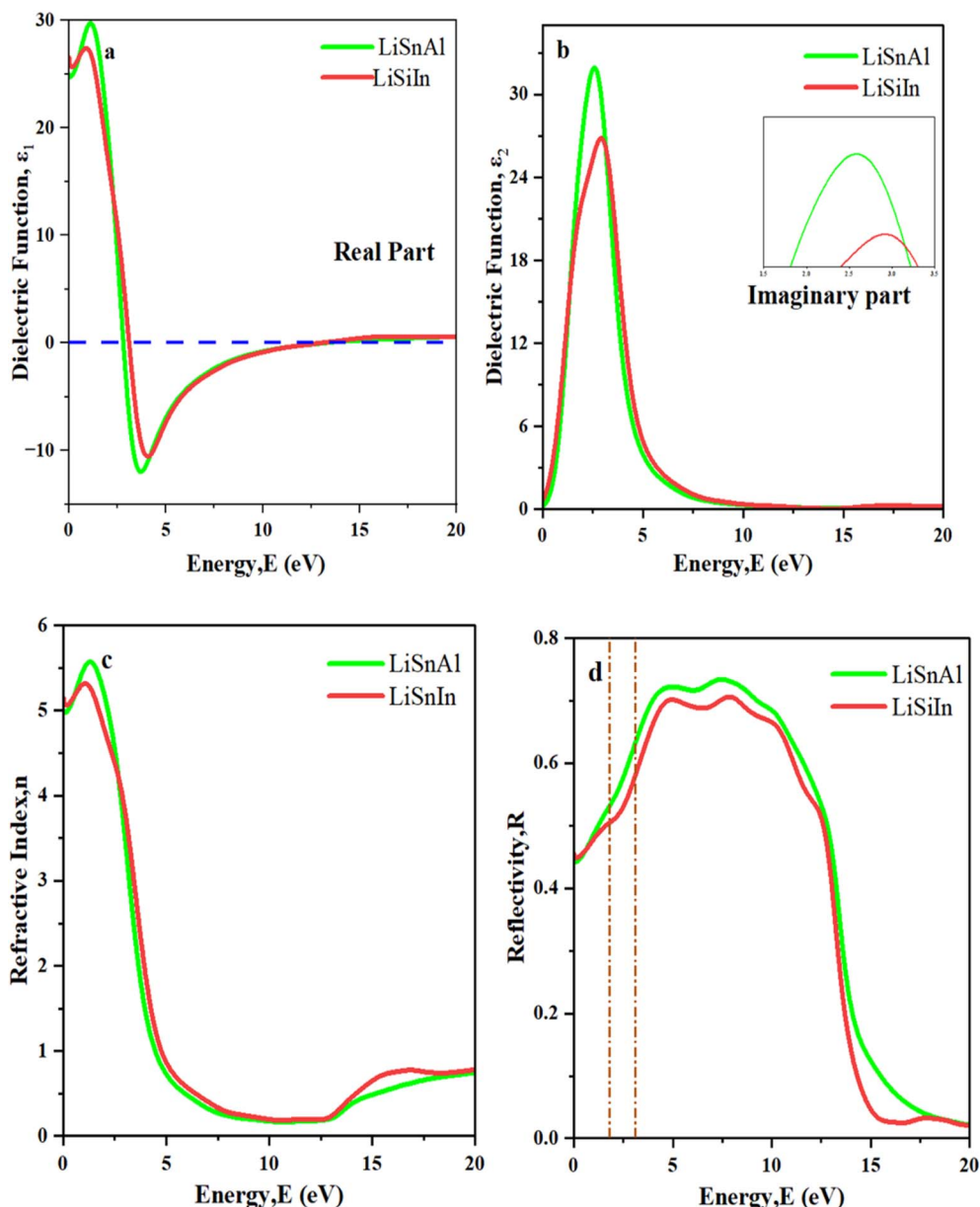


Fig. 6 Photon energy dependence of (a) real  $\epsilon_1$ , (b) imaginary part of dielectric function  $\epsilon_2$ , (c) refractive index  $n$ , (d) reflectivity  $R$  of LiSnAl and LiSiIn.

### 3.6 Thermodynamic properties

A comprehensive understanding of thermodynamic behavior is essential for evaluating the potential of materials in high-temperature and energy-efficient applications. Following the phonon calculations performed, we investigated key thermodynamic parameters including the Debye temperature ( $\theta_D$ ), minimum thermal conductivity, Dulong–Petit limit, average sound velocity, melting temperature, specific heat capacity, entropy, and thermal expansion coefficient. These properties were calculated within the framework of the quasi-harmonic approximation (QHA),<sup>52</sup> which extends beyond the harmonic approximation (HA) by incorporating the volume dependence of phonon frequencies. Unlike the HA, which assumes infinite phonon lifetimes and neglects phonon–phonon interactions,

QHA enables the inclusion of thermal expansion and anharmonic effects to a limited extent. Although QHA does not fully capture strong anharmonicity above  $\sim 1000$  K, it remains accurate and reliable for the temperature range considered in this study (100–900 K). All calculations were conducted under zero external pressure, and the temperature range spanned from 10 to 800 K. The phonon dispersion curves, shown in Fig. 9, were analyzed to verify the dynamic stability of the compounds.

The Debye temperature ( $\theta_D$ ), a fundamental thermodynamic parameter related to lattice vibrations and thermal conductivity, was computed using the following relation,<sup>53</sup>

$$\Theta_D = \frac{h}{2\pi k_B} \left( \frac{3n}{4\pi} \times \frac{N_A}{M} \rho \right) \quad (3.13)$$



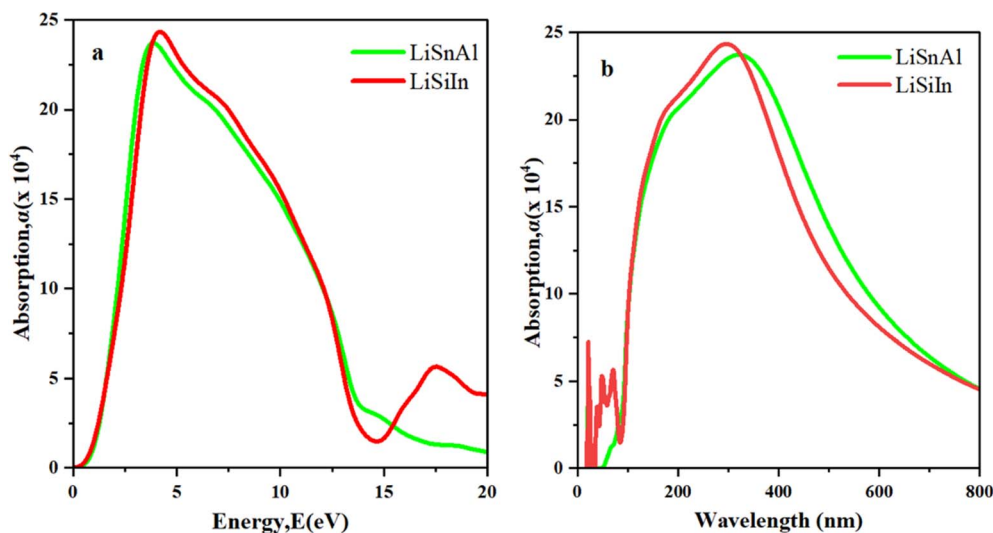


Fig. 7 Optical properties (a) and (b) absorption of LiSnAl and LiSiIn at the polarization vector [100].

Here,  $h$  is Planck's constant,  $k_B$  is Boltzmann's constant,  $n$  is the number of atoms per formula unit,  $N_A$  is Avogadro's number,  $M$  is the molar mass, and  $\rho$  is the material's density.

The average sound velocity ( $V_m$ ) was derived from the longitudinal ( $V_p$ ) and transverse ( $V_G$ ) sound velocities, as expressed in the following equations,<sup>53</sup>

$$V_m = \sqrt[3]{\frac{2}{V_G^3} + \frac{1}{V_p^3}}^{-1/3} \quad (3.14)$$

$$V_p = \sqrt{\frac{3B + 4G}{3\rho}} \quad (3.15)$$

$$V_G = \sqrt{\frac{G}{\rho}} \quad (3.16)$$

where  $B$  and  $G$  denote the bulk and shear moduli, respectively.

The minimum thermal conductivity ( $K_{\min}$ ) is calculated using the following equations.<sup>54,55</sup> They are essential physical parameters for practical applications of a material.

$$K_{\min} = K_B \nu_m \left( \frac{M}{n\rho N_A} \right)^{-2/3} \quad (3.17)$$

The melting temperature ( $T_m$ ) was estimated using the empirical relation,<sup>56</sup>

$$T_m = 553 + 5.91C_{11} \pm 300 \text{ k} \quad (3.18)$$

The coefficient of thermal expansion ( $\alpha$ ) was calculated using:

$$\alpha = \frac{1.6 \times 10^{-3}}{G} \quad (3.19)$$

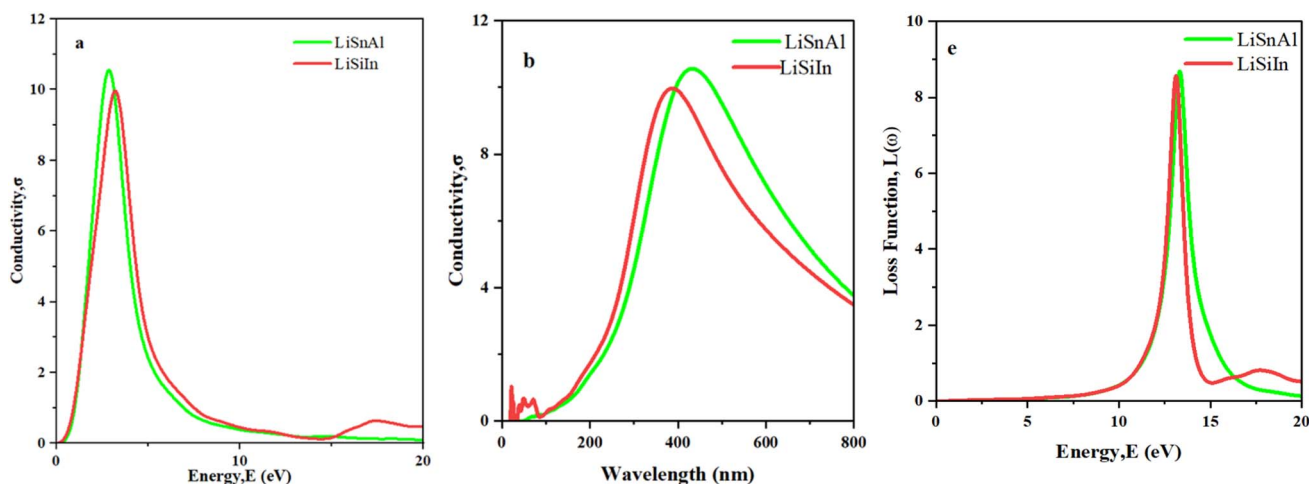


Fig. 8 Optical properties (a) and (b) conductivity and (c) loss function of LiSnAl and LiSiIn at the polarization vector [100].



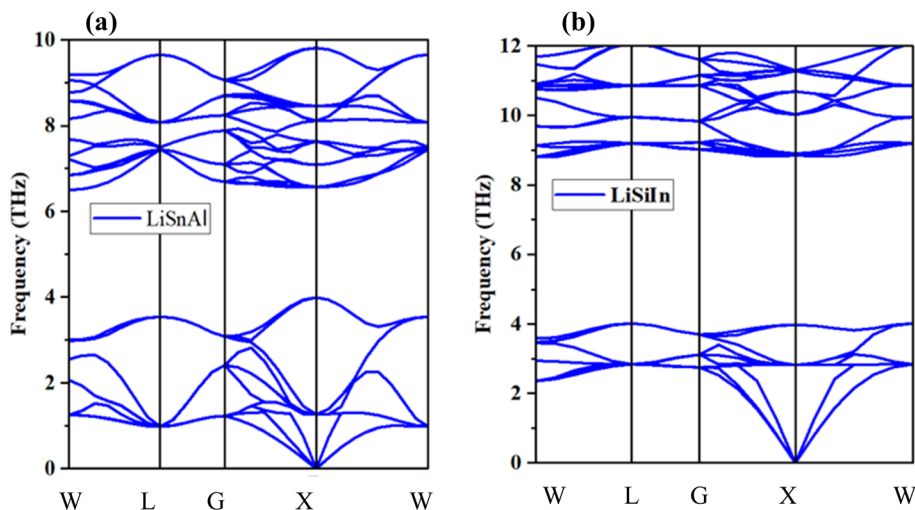


Fig. 9 The Phonon dispersion spectra of the compounds (a) LiSnAl and (b) LiSiIn.

These thermodynamic parameters, displayed in Table 4, are vital for the design of devices operating across variable thermal regimes and for improving energy efficiency in practical applications.

The phonon dispersion spectra of LiSiIn and LiSnAl confirm the dynamic stability of both compounds, as evidenced by the absence of imaginary frequencies, shown in Fig. 9. The phonon branches can be categorized into acoustic and optical modes. The acoustic modes—longitudinal acoustic (LA), transverse acoustic (TA), and shear acoustic (SA)—originate from the  $\Gamma$ -point and represent collective in-phase atomic vibrations. These modes, typically located in the low-frequency region (0–3 THz), significantly determine thermal conductivity. Conversely, optical phonon modes arise from out-of-phase vibrations between atoms of differing masses and are observed at higher frequencies (above 4 THz). Notably, LiSiIn displays marginally higher optical mode frequencies compared to LiSnAl. This can be attributed to the presence of the heavier Sn atom in LiSnAl, which results in vibrational softening. The separation between acoustic and optical branches reflects disparities in atomic masses and bonding stiffness, both of which influence the thermal and optical responses of the material. Furthermore, the phonon dispersions provide insight into phonon–phonon

interactions, which are critical for evaluating the thermoelectric performance of materials. The results indicate that both compounds exhibit thermodynamic stability and favorable thermal characteristics suitable for high-temperature and energy-related applications.

The Debye temperatures for LiSnAl and LiSiIn were calculated to be 350.23 K and 386.34 K, respectively. Fig. 10(a) illustrates the temperature-dependent variation of Debye temperature over the range of 10–800 K. A distinct temperature dependence is observed particularly in the lower temperature region (10–250 K), beyond which the Debye temperature begins to plateau. It is important to note that quantum mechanical effects, while diminishing near the Debye temperature, play a critical role in determining the thermodynamic behavior of materials at temperatures below this threshold.<sup>57,58</sup> Based on the Debye temperature analysis, LiSiIn is anticipated to possess superior electrical conductivity due to its higher  $\theta_D$ . Conversely, at low temperatures ( $T \ll \theta_D$ ), LiSnAl, with a lower Debye temperature, is expected to exhibit greater values of specific heat and entropy. However, as the temperature increases and approaches the Debye temperature, both compounds display saturation behavior in their specific heat and entropy values, as shown in Fig. 10(b) and (c).

For clarity and comparison, especially when plotting thermodynamic properties, entropy is often represented as the product  $S^*T$ , which directly relates to enthalpy (H) in thermodynamics. Enthalpy reflects the total internal energy of a system due to thermal excitation. A higher enthalpy implies greater energy dispersion with temperature, whereas a lower enthalpy indicates limited energy distribution. According to the entropy trends shown in Fig. 10(c), LiSiIn shows a higher enthalpy than LiSnAl, suggesting more significant thermal energy distribution.

Thermal expansion coefficient ( $\alpha$ ) is another key parameter that impacts structural reliability during thermal cycling. Lower values of  $\alpha$  reduce mechanical stress accumulation, thereby enhancing structural stability. This factor is essential in

**Table 4** Calculated longitudinal ( $V_p$  in  $\text{m s}^{-1}$ ), transverse ( $V_G$  in  $\text{m s}^{-1}$ ), average sound velocity ( $V_m$  in  $\text{m s}^{-1}$ ), Debye temperature ( $\theta_D$  in K), melting temperature ( $T_m$  in K), Minimum thermal conductivity ( $K_{\min}$ ), Thermal expansion coefficient ( $\alpha$ ) for the compounds LiSnAl and LiSiIn

| Parameter               | LiSnAl  | LiSiIn  |
|-------------------------|---------|---------|
| $\rho$                  | 3.74    | 4.01    |
| $V_p$                   | 4887.41 | 5101.46 |
| $V_G$                   | 3036.76 | 3253.61 |
| $V_m$                   | 3347.41 | 3576.07 |
| $\theta_D$              | 350.23  | 386.34  |
| $T_m$                   | 1003.46 | 1100.02 |
| $K_{\min}$              | 0.006   | 0.007   |
| $\alpha \times 10^{-5}$ | 4.64    | 3.77    |



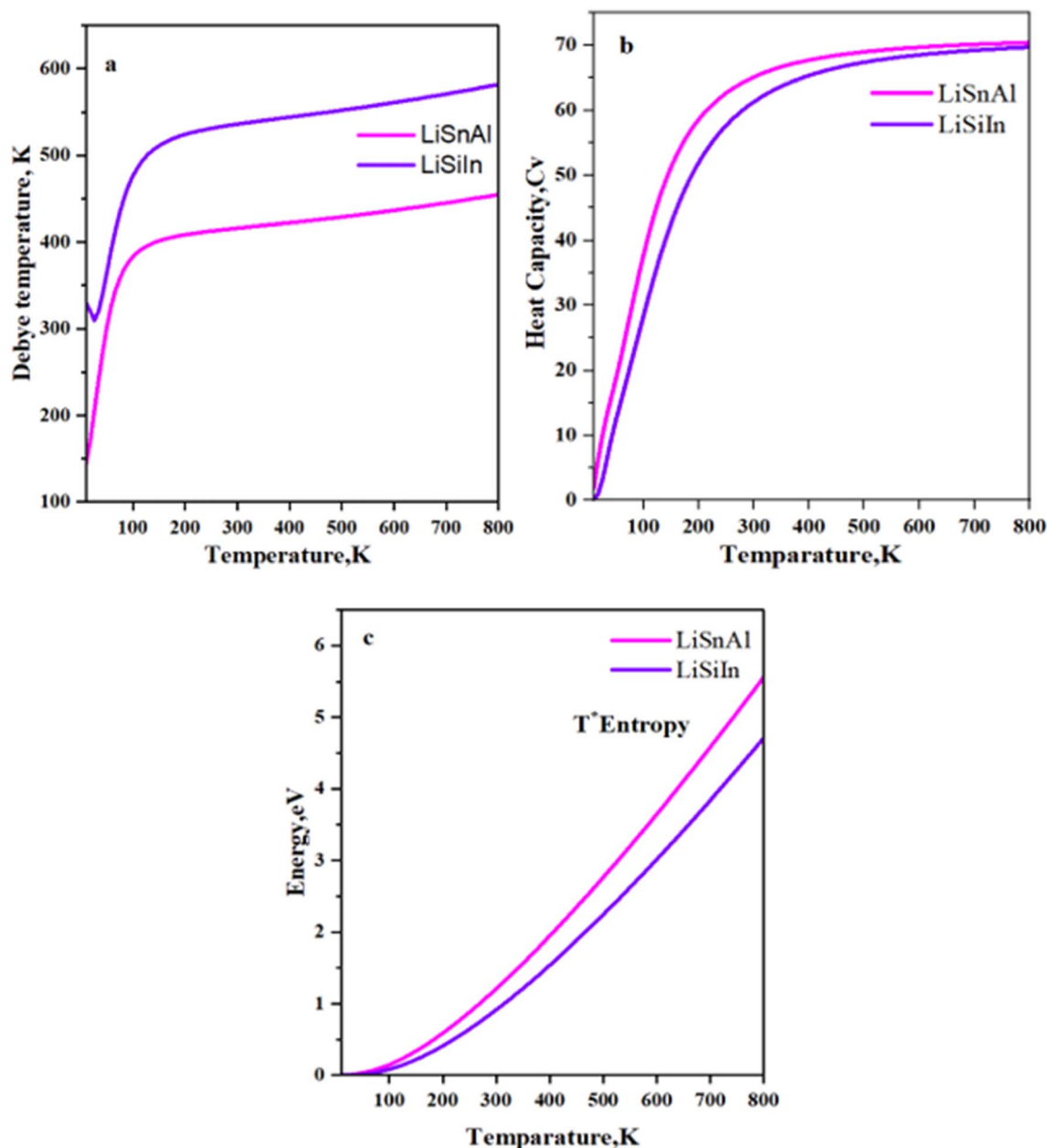


Fig. 10 The calculated thermodynamic properties (a) Debye temperature, (b) heat capacity ( $C_v$ ), and (c) entropy with respect to internal energy.

thermal management for solid-state refrigeration and thermoelectric applications. The comparative analysis of melting temperatures, as reported in Table 4, confirms that LiSnAl has a lower melting point than LiSiIn. Furthermore, the data indicate an inverse relationship between melting temperature and thermal expansion coefficient, following the relation  $\alpha \approx \frac{0.2}{T_m}$ . This trend suggests that LiSiIn, with its higher melting temperature, exhibits a correspondingly lower thermal expansion coefficient, which is advantageous for epitaxial crystal growth and integration in electronic and spintronic devices.<sup>50,58</sup>

Low thermal conductivity is a desirable trait in thermoelectric materials, as it aids in maintaining a strong temperature gradient across the device, thereby improving efficiency.<sup>51</sup> As shown in

Table 4, both LiSnAl and LiSiIn exhibit low values of minimum thermal conductivity, which makes them promising candidates for solid-state refrigeration and thermoelectric applications. Specifically, LiSnAl's lower thermal conductivity could lead to improved thermoelectric performance, while LiSiIn, due to its higher Debye and melting temperatures, demonstrates strong potential for use in high-temperature environments.

## 4 Conclusions

This work employed DFT-based first-principles calculations to comprehensively investigate the structural, mechanical, electronic, optical, charge density, and thermodynamic properties of the non-magnetic, p-type half-Heusler compounds LiSiIn and

LiSnAl. To the best of our knowledge, this is the first report to explore these properties using the CASTEP simulation framework. The calculated lattice constants show excellent agreement with previously reported values, validating the reliability of the computational approach. Both LiSnAl and LiSiIn have indirect and narrow band gaps, calculated at 0.095 eV and 0.228 eV for GGA-PBE functional and 0.517 eV and 0.591 eV for the Hybrid-HSE06 functional. Elastic constants confirm that both compounds satisfy Born's mechanical stability criteria, with LiSiIn exhibiting marginally superior elasticity. The band structure analysis reveals that both materials possess direct and relatively narrow band gaps, indicating semiconducting behavior. Charge density distributions and Mulliken population analysis reveal a mixed ionic-covalent bonding nature, further supported by effective valence calculations. The negative Cauchy pressure confirms the brittle and covalent character of both compounds. Optical analysis suggests that the high dielectric constants and ultraviolet reflectivity make these materials suitable for applications in capacitors, IR detectors and thermophotovoltaics devices. Thermodynamic stability is affirmed by phonon dispersion calculations, while thermal property evaluations indicate that LiSiIn exhibits a higher melting temperature (1100.02 K) compared to LiSnAl (1003.46 K), implying stronger interatomic bonding. However, the minimum thermal conductivity ( $K_{\min}$ ) of LiSnAl ( $\sim 0.006 \text{ W m}^{-1} \text{ K}^{-1}$ ) compared to LiSiIn ( $\sim 0.007 \text{ W m}^{-1} \text{ K}^{-1}$ ) suggests that it may be more effective for applications requiring thermal insulation or energy storage. Overall, both LiSiIn and LiSnAl demonstrate promising potential for future applications in thermoelectric devices.

## Author contributions

Mohshina Binte Mansur: conceptualization, methodology, software, validation, investigation, data curation, writing – original draft, visualization. Tasmi Akter: investigation, writing – original draft, formal analysis. Istiak Ahmed Ovi: visualization, project administration, formal analysis, data curation, writing – review & editing. Jahirul Islam: conceptualization, writing – review & editing, software, resources, supervision. Wahidur Rahman Sajal: conceptualization, writing – review & editing, validation, resources, supervision.

## Conflicts of interest

The authors declare that they have no known financial or personal conflicts of interest that could have impacted on the findings of this study.

## Data availability

Data will be available upon request.

## Acknowledgements

This research was undertaken at the Computational Materials Science Laboratory, which is part of the Department of

Materials Science and Engineering at Khulna University of Engineering & Technology, Khulna-9203, Bangladesh.

## References

- 1 M. D. Ratul Hasan, I. A. Apon, I. Ahmed Ovi and F.-T. -Zahra, Impact of Applied Pressure on Tin-Based Cubic Halide Perovskite  $\text{ASnX}_3$  ( $A = \text{Li, Na}$  and  $X = \text{Cl, Br, and I}$ ) in Reference to Their Optoelectronic Applications, *Int. J. Energy Res.*, 2024, **2024**, 8213804, DOI: [10.1155/2024/8213804](https://doi.org/10.1155/2024/8213804).
- 2 O. Caballero-Calero, J. R. Ares and M. Martín-González, Environmentally Friendly Thermoelectric Materials: High Performance from Inorganic Components with Low Toxicity and Abundance in the Earth, *Adv. Sustainable Syst.*, 2021, **5**, 2100095, DOI: [10.1002/advs.202100095](https://doi.org/10.1002/advs.202100095).
- 3 S. Ning, S. Huang, Z. Zhang, R. Zhang, N. Qi and Z. Chen, High thermoelectric performance of topological half-Heusler compound  $\text{LaPtBi}$  achieved by hydrostatic pressure, *Phys. Chem. Chem. Phys.*, 2020, **22**, 14621–14629, DOI: [10.1039/D0CP01442G](https://doi.org/10.1039/D0CP01442G).
- 4 F. Parvin, M. A. Hossain, I. Ahmed, K. Akter and A. K. M. A. Islam, First-principles calculations to investigate mechanical, optoelectronic and thermoelectric properties of half-Heusler p-type semiconductor  $\text{BaAgP}$ , *Results Phys.*, 2021, **23**, 104068, DOI: [10.1016/j.rinp.2021.104068](https://doi.org/10.1016/j.rinp.2021.104068).
- 5 M. Husain, N. Rahman, N. Sfina, T. Zaman, N. H. Al-Shaalan, S. Alharthi, S. A. Alharthy, M. A. Amin, R. Khan, M. Sohail, M. M. Ramli and A. H. Reshak, DFT-based computational investigations of the structural, electronic, elastic, and magnetic properties of ternary Half-Heusler  $\text{TiVX}$  ( $X = \text{Ge, Si, Pb, Sn}$ ) compounds, *Chin. J. Phys.*, 2024, **89**, 1819–1826, DOI: [10.1016/j.cjph.2023.09.007](https://doi.org/10.1016/j.cjph.2023.09.007).
- 6 B. Jiang, W. Wang, S. Liu, Y. Wang, C. Wang, Y. Chen, L. Xie, M. Huang and J. He, High figure-of-merit and power generation in high-entropy  $\text{GeTe}$ -based thermoelectrics, *Science*, 2022, **377**, 208–213, DOI: [10.1126/science.abq5815](https://doi.org/10.1126/science.abq5815).
- 7 O. Meroz, N. Elkabets and Y. Gelbstein, Enhanced Thermoelectric Properties of n-Type  $\text{Bi}_2\text{Te}_3$ - $x\text{Sex}$  Alloys following Melt-Spinning, *ACS Appl. Energy Mater.*, 2020, **3**, 2090–2095, DOI: [10.1021/acsam.9b02133](https://doi.org/10.1021/acsam.9b02133).
- 8 H.-T. Liu, Q. Sun, Y. Zhong, Q. Deng, L. Gan, F.-L. Lv, X.-L. Shi, Z.-G. Chen and R. Ang, High-performance in n-type  $\text{PbTe}$ -based thermoelectric materials achieved by synergistically dynamic doping and energy filtering, *Nano Energy*, 2022, **91**, 106706, DOI: [10.1016/j.nanoen.2021.106706](https://doi.org/10.1016/j.nanoen.2021.106706).
- 9 D. Ben-Ayoun, Y. Sadia and Y. Gelbstein, Compatibility between Co-Metallized  $\text{PbTe}$  Thermoelectric Legs and an Ag-Cu-In Brazing Alloy, *Materials*, 2018, **11**, 99, DOI: [10.3390/ma11010099](https://doi.org/10.3390/ma11010099).
- 10 M. Kaller, D. Fuks and Y. Gelbstein, Sc solubility in p-type half-Heusler ( $\text{Ti1-cSc}$ ) $\text{NiSn}$  thermoelectric alloys, *J. Alloys Compd.*, 2017, **729**, 446–452, DOI: [10.1016/j.jallcom.2017.09.137](https://doi.org/10.1016/j.jallcom.2017.09.137).



- 11 Vikram, B. Sahni, C. K. Barman and A. Alam, Accelerated Discovery of New 8-Electron Half-Heusler Compounds as Promising Energy and Topological Quantum Materials, *J. Phys. Chem. C*, 2019, **123**, 7074–7080, DOI: [10.1021/acs.jpcc.9b01737](https://doi.org/10.1021/acs.jpcc.9b01737).
- 12 R. M. Sattigeri and P. K. Jha, Dimensional engineering of a topological insulating phase in Half-Heusler LiMgAs, *Sci. Rep.*, 2021, **11**, 6432, DOI: [10.1038/s41598-021-85806-1](https://doi.org/10.1038/s41598-021-85806-1).
- 13 M. Miri, Y. Ziat, H. Belkhanchi, Z. Zarhri and Y. Ait El Kadi, Structural and optoelectronic properties of LiYP ( $Y = Ca, Mg,$  and  $Zn$ ) half-Heusler alloy under pressure: A DFT study, *Phys. Rev. B*, 2023, **667**, 415216, DOI: [10.1016/j.physb.2023.415216](https://doi.org/10.1016/j.physb.2023.415216).
- 14 Y. Benazouzi, H. Rozale, M. A. Boukli Hacene, M. Khethir, A. Chahed and D. Lucache, Electronic and Thermoelectric Properties in Li-Based Half-Heusler Compounds: A First Principle Study, *Ann. West Univ. Timiș., Phys. Ser.*, 2019, **61**, 44–55, DOI: [10.2478/awutp-2019-0004](https://doi.org/10.2478/awutp-2019-0004).
- 15 A. Roy, J. W. Bennett, K. M. Rabe and D. Vanderbilt, Half-Heusler Semiconductors as Piezoelectrics, *Phys. Rev. Lett.*, 2012, **109**, 037602, DOI: [10.1103/PhysRevLett.109.037602](https://doi.org/10.1103/PhysRevLett.109.037602).
- 16 T. Graf, C. Felser and S. S. P. Parkin, Simple rules for the understanding of Heusler compounds, *Prog. Solid State Chem.*, 2011, **39**, 1–50, DOI: [10.1016/j.progsolidstchem.2011.02.001](https://doi.org/10.1016/j.progsolidstchem.2011.02.001).
- 17 L. Huang, Q. Zhang, B. Yuan, X. Lai, X. Yan and Z. Ren, Recent progress in half-Heusler thermoelectric materials, *Mater. Res. Bull.*, 2016, **76**, 107–112, DOI: [10.1016/j.materresbull.2015.11.032](https://doi.org/10.1016/j.materresbull.2015.11.032).
- 18 M. Javed, M. A. Sattar, M. Benkraouda and N. Amrane, First-principles investigations on the structural stability, thermophysical and half-metallic properties of the half-Heusler CrMnS alloy, *Opt. Quantum Electron.*, 2021, **54**, 1, DOI: [10.1007/s11082-021-03373-1](https://doi.org/10.1007/s11082-021-03373-1).
- 19 F. Soyalt, G. Ugur, Ş. Uğur, H. C. Şen and R. Ellialtıoglu, A first-principles study of the structural, elastic, electronic and phonon properties of LiMgP and LiMgAs in the  $\alpha$ ,  $\beta$  and  $\gamma$  phases, *J. Alloys Compd.*, 2013, **551**, 108–117, DOI: [10.1016/j.jallcom.2012.09.110](https://doi.org/10.1016/j.jallcom.2012.09.110).
- 20 R. Kurchania, U. Namdeo, Y. Jain and D. Shrivastava, Analysing the structural, mechanical and thermal stability in lithium-based half-Heusler compounds LiAlSi and LiAlGe: a first-principles study, *Bull. Mater. Sci.*, 2023, **46**, 117, DOI: [10.1007/s12034-023-02956-w](https://doi.org/10.1007/s12034-023-02956-w).
- 21 Y. Gupta, M. M. Sinha and S. S. Verma, Investigations of mechanical and thermoelectric properties of 'AlNiP' novel half-Heusler alloy, *Mater. Chem. Phys.*, 2021, **265**, 124518, DOI: [10.1016/j.matchemphys.2021.124518](https://doi.org/10.1016/j.matchemphys.2021.124518).
- 22 M. Islam and A. R. Sheikh, A comprehensive DFT study on the physical properties of XCrAl ( $X = Fe, Co, Ni, Cu$ ) half-Heusler alloys for applications in high-temperature technology, *Phys. Rev. B*, 2023, **668**, 415244, DOI: [10.1016/j.physb.2023.415244](https://doi.org/10.1016/j.physb.2023.415244).
- 23 A. Amudhavalli, R. Rajeswarapalanichamy, K. Iyakutti and A. K. Kushwaha, First principles study of structural and optoelectronic properties of Li based half Heusler alloys, *Comput. Condens. Matter*, 2018, **14**, 55–66, DOI: [10.1016/j.cocom.2018.01.002](https://doi.org/10.1016/j.cocom.2018.01.002).
- 24 Q.-Q. Liang, D.-Y. Hu, T.-Y. Tang, H.-X. Gao, S.-Q. Wu, L. Li and Y.-L. Tang, First-principles calculations to investigate structural, electronic, optical and thermodynamic properties of anti-perovskite compounds X3OI ( $X = Na, K, Rb$ ), *J. Mater. Res. Technol.*, 2023, **22**, 3245–3254, DOI: [10.1016/j.jmrt.2022.12.148](https://doi.org/10.1016/j.jmrt.2022.12.148).
- 25 First principles methods using CASTEP, <https://www.degruyter.com/document/doi/10.1524/zkri.220.5.567.65075/html>, accessed May 23, 2024.
- 26 R. Srivastava, Application of Optimization Algorithms in Clusters, *Front. Chem.*, 2021, **9**, 637286, DOI: [10.3389/fchem.2021.637286](https://doi.org/10.3389/fchem.2021.637286).
- 27 Y. Wang, P. Wisesa, A. Balasubramanian, S. Dwaraknath and T. Mueller, Rapid generation of optimal generalized Monkhorst-Pack grids, *Comput. Mater. Sci.*, 2021, **187**, 110100, DOI: [10.1016/j.commatsci.2020.110100](https://doi.org/10.1016/j.commatsci.2020.110100).
- 28 A. K. Kushwaha, A. Haddou, S. P. Mishra, S. Chauhan, R. Khenata, R. Ahmed, S. Bin Omran and A. Bouhemadou, Theoretical investigation of phonon modes related to first Brillouin zone centre and properties of double perovskites Ba2MWO6 ( $M = Mg, Zn, Cd$ ), *Comput. Condens. Matter*, 2023, **34**, e00758, DOI: [10.1016/j.cocom.2022.e00758](https://doi.org/10.1016/j.cocom.2022.e00758).
- 29 D. Shrivastava and S. P. Sanyal, Theoretical study of structural, electronic, phonon and thermoelectric properties of KScX ( $X = Sn$  and  $Pb$ ) and KYX ( $X = Si$  and  $Ge$ ) half-Heusler compounds with 8 valence electrons count, *J. Alloys Compd.*, 2019, **784**, 319–329, DOI: [10.1016/j.jallcom.2019.01.050](https://doi.org/10.1016/j.jallcom.2019.01.050).
- 30 The Structural, Magnetic, Optoelectronic, and Mechanical Characteristics of NaGeX3 Perovskites Under Pressure for Solar-Cell Applications - IOPscience, <https://iopscience.iop.org/article/10.1088/2053-1591/ad594d/meta>, accessed June 24, 2024.
- 31 S. Chen, K. C. Lukas, W. Liu, C. P. Opeil, G. Chen and Z. Ren, Effect of Hf Concentration on Thermoelectric Properties of Nanostructured N-Type Half-Heusler Materials HfxZr<sub>1-x</sub>NiSn<sub>0.995</sub>b<sub>0.01</sub>, *Adv. Energy Mater.*, 2013, **3**, 1210–1214, DOI: [10.1002/aenm.201300336](https://doi.org/10.1002/aenm.201300336).
- 32 M. I. Naher and S. H. Naqib, An *ab-initio* study on structural, elastic, electronic, bonding, thermal, and optical properties of topological Weyl semimetal TaX ( $X = P, As$ ), *Sci. Rep.*, 2021, **11**, 5592, DOI: [10.1038/s41598-021-85074-z](https://doi.org/10.1038/s41598-021-85074-z).
- 33 R. S. Mulliken, Electronic Population Analysis on LCAO-MO Molecular Wave Functions. III. Effects of Hybridization on Overlap and Gross AO Populations, *J. Chem. Phys.*, 1955, **23**, 2338–2342, DOI: [10.1063/1.1741876](https://doi.org/10.1063/1.1741876).
- 34 M. A. Hadi, S. H. Naqib, S.-R. G. Christopoulos, A. Chronos and A. K. M. A. Islam, Mechanical behavior, bonding nature and defect processes of Mo2ScAlC2: A new ordered MAX phase, *J. Alloys Compd.*, 2017, **724**, 1167–1175, DOI: [10.1016/j.jallcom.2017.07.110](https://doi.org/10.1016/j.jallcom.2017.07.110).
- 35 M. Born, On the stability of crystal lattices. I, *Math. Proc. Cambridge Philos. Soc.*, 1940, **36**, 160–172, DOI: [10.1017/S0305004100017138](https://doi.org/10.1017/S0305004100017138).
- 36 V. A. Koptsik, Generalized Symmetry in Crystal Physics, in *Cryst. Symmetries*, ed. I. Hargittai and B. K. Vainshtein,



- Pergamon, Amsterdam, 1988, pp. 407–424, DOI: [10.1016/B978-0-08-037014-9.50013-3](https://doi.org/10.1016/B978-0-08-037014-9.50013-3).
- 37 Md. L. Ali and Md. Z. Rahaman, Investigation of different physical aspects such as structural, mechanical, optical properties and Debye temperature of Fe<sub>2</sub>ScM (M=P and As) semiconductors: A DFT-based first principles study, *Int. J. Mod. Phys. B*, 2018, **32**, 1850121, DOI: [10.1142/S0217979218501217](https://doi.org/10.1142/S0217979218501217).
- 38 M. A. Hadi, M. Dahlqvist, S.-R. G. Christopoulos, S. H. Naqib, A. Chroneos and A. K. M. A. Islam, Chemically stable new MAX phase V<sub>2</sub>SnC: a damage and radiation tolerant TBC material, *RSC Adv.*, 2020, **10**, 43783–43798, DOI: [10.1039/D0RA07730E](https://doi.org/10.1039/D0RA07730E).
- 39 K. Kaur, D. P. Rai, R. K. Thapa and S. Srivastava, Structural, electronic, mechanical, and thermoelectric properties of a novel half Heusler compound HfPtPb, *J. Appl. Phys.*, 2017, **122**, 045110, DOI: [10.1063/1.4996648](https://doi.org/10.1063/1.4996648).
- 40 F. Fakhera, N. Ahnaf Shahed, S. Khanom, M. K. Hossain and F. Ahmed, The first-principle study on structural, mechanical, electronic and optical properties of half-metallic CaMSi<sub>2</sub>O<sub>6</sub> (M= Co, Fe, Mn) clinopyroxenes, *Comput. Condens. Matter*, 2022, **33**, e00749, DOI: [10.1016/j.cocom.2022.e00749](https://doi.org/10.1016/j.cocom.2022.e00749).
- 41 M. I. Naher and S. H. Naqib, Structural, elastic, electronic, bonding, and optical properties of topological CaSn<sub>3</sub> semimetal, *J. Alloys Compd.*, 2020, **829**, 154509, DOI: [10.1016/j.jallcom.2020.154509](https://doi.org/10.1016/j.jallcom.2020.154509).
- 42 E. Haque and M. A. Hossain, Elastic, magnetic, transport and electronic properties of noncentrosymmetric M<sub>2</sub>Mo<sub>3</sub>N (M = Fe, Co, Ni, Rh): A first-principles study, *J. Alloys Compd.*, 2018, **748**, 117–126, DOI: [10.1016/j.jallcom.2018.03.151](https://doi.org/10.1016/j.jallcom.2018.03.151).
- 43 M. T. Hossain, J. Islam, M. Hasan and K. Hossain, First-principles calculation to investigate electronic, optical, and mechanical properties of halide perovskite LiABr<sub>3</sub> (A = Ca, Sr, and Ba) for optoelectronic technologies, *Phys. Rev. B*, 2024, **691**, 416355, DOI: [10.1016/j.physb.2024.416355](https://doi.org/10.1016/j.physb.2024.416355).
- 44 Calculations of the Mechanical, Optoelectronic, and Magnetic Properties of FrGeX<sub>3</sub> (X = Cl, Br, I) under Hydrostatic Pressures Based on First-Principles Theories, *AIP Advances*, AIP Publishing, <https://pubs.aip.org/aip/adv/article/14/3/035341/3277997>, accessed May 23, 2024.
- 45 M. Saiduzzaman, T. Ahmed, K. M. Hossain, A. Biswas, S. K. Mitro, A. Sultana, M. S. Alam and S. Ahmad, Band gap tuning of non-toxic Sr-based perovskites CsSrX<sub>3</sub> (X = Cl, Br) under pressure for improved optoelectronic applications, *Mater. Today Commun.*, 2023, **34**, 105188, DOI: [10.1016/j.mtcomm.2022.105188](https://doi.org/10.1016/j.mtcomm.2022.105188).
- 46 M. Husain, H. Albalawi, M. A. Huwayz, R. Khan and N. Rahman, First-principle computation of some physical properties of half-Heusler compounds for possible thermoelectric applications, *RSC Adv.*, 2023, **13**, 23716–23727, DOI: [10.1039/D3RA04192A](https://doi.org/10.1039/D3RA04192A).
- 47 W. A. Dujana, A. Podder, O. Das, Md. Solayman, M. T. Nasir, M. A. Rashid, M. Saiduzzaman and M. A. Hadi, Structural, electronic, mechanical, thermal, and optical properties of UIr<sub>3</sub> under pressure: A comprehensive DFT study, *AIP Adv.*, 2021, **11**, 105205, DOI: [10.1063/5.0064021](https://doi.org/10.1063/5.0064021).
- 48 R. Ahmad and N. Mehmood, A Density Functional Theory Investigations of Half-Heusler Compounds RhVZ (Z = P, As, Sb), *J. Supercond. Novel Magn.*, 2018, **31**, 1577–1586, DOI: [10.1007/s10948-017-4370-4](https://doi.org/10.1007/s10948-017-4370-4).
- 49 Pressure-driven semiconducting to metallic transition in francium tin trihalides perovskite with improved optoelectronic performance: A DFT study, *AIP Advances*, AIP Publishing, <https://pubs.aip.org/aip/adv/article/14/6/065126/3298110>, accessed June 24, 2024.
- 50 M. I. Naher and S. H. Naqib, First-principles insights into the mechanical, optoelectronic, thermophysical, and lattice dynamical properties of binary topological semimetal BaGa<sub>2</sub>, *Results Phys.*, 2022, **37**, 105507, DOI: [10.1016/j.rinp.2022.105507](https://doi.org/10.1016/j.rinp.2022.105507).
- 51 I. Kars Durukan and Y. Oztekin Ciftci, First-principles calculations of vibrational and optical properties of half-Heusler NaScSi, *Indian J. Phys.*, 2021, **95**, 2303–2312, DOI: [10.1007/s12648-020-01887-0](https://doi.org/10.1007/s12648-020-01887-0).
- 52 A. Togo and I. Tanaka, First principles phonon calculations in materials science, *Scr. Mater.*, 2015, **108**, 1–5, DOI: [10.1016/j.scriptamat.2015.07.021](https://doi.org/10.1016/j.scriptamat.2015.07.021).
- 53 O. L. Anderson, A simplified method for calculating the debye temperature from elastic constants, *J. Phys. Chem. Solids*, 1963, **24**, 909–917, DOI: [10.1016/0022-3697\(63\)90067-2](https://doi.org/10.1016/0022-3697(63)90067-2).
- 54 D. T. Morelli and G. A. Slack, High Lattice Thermal Conductivity Solids, in *High Therm. Conduct. Mater.*, ed. S. L. Shindé and J. S. Goela, Springer, New York, NY, 2006, pp. 37–68, DOI: [10.1007/0-387-25100-6\\_2](https://doi.org/10.1007/0-387-25100-6_2).
- 55 D. R. Clarke, Materials selection guidelines for low thermal conductivity thermal barrier coatings, *Surf. Coat. Technol.*, 2003, **163–164**, 67–74, DOI: [10.1016/S0257-8972\(02\)00593-5](https://doi.org/10.1016/S0257-8972(02)00593-5).
- 56 Md. A. U. Islam, Md. R. Islam, O. das, S. Kato, N. Kishi and T. Soga, First-Principles Calculations to Investigate the Stability and Thermodynamic Properties of a Newly Exposed Lithium–Gallium–Iridium-Based Full-Heusler Compound, *ACS Omega*, 2023, **8**, 21885–21897, DOI: [10.1021/acsomega.3c01534](https://doi.org/10.1021/acsomega.3c01534).
- 57 S. A. Sofi and D. C. Gupta, High temperature and pressure study on structural and thermophysical properties of Co<sub>2</sub>XAl (X = Zr, Nb, Hf) Heusler materials by density functional theory calculations, *Philos. Mag.*, 2021, **101**, 1654–1678, DOI: [10.1080/14786435.2021.1917783](https://doi.org/10.1080/14786435.2021.1917783).
- 58 M. Y. Raiã, R. Masrour, A. Jabar, M. Hamedoun, A. Rezzouk, A. Hourmatallah, N. Benzakour, K. Bouslykhane and J. Kharbach, Investigations of martensitic, thermodynamics, elastic, electronic, magnetic, thermal and thermoelectric properties of Co<sub>2</sub>FeZ Heusler alloys (Z=Si; Ge; Al; Ga): a first principle study, *Mol. Phys.*, 2022, **120**, e2075289, DOI: [10.1080/00268976.2022.2075289](https://doi.org/10.1080/00268976.2022.2075289).

